Journal of
Materials Chemistry A

ROYAL SOCIETY
OF CHEMISTRY

PAPER

View Article Online
View Journal

Cite this: DOI: 10.1039/d5ta10393b

Incorporating chrysene units to improve the performance of poly(arylene piperidinium) and poly(arylene quinuclidinium) anion exchange membranes for water electrolysis

Triet Nguyen Dai Luong and Patric Jannasch *

Received 21st December 2025
Accepted 16th March 2026

DOI: 10.1039/d5ta10393b

rsc.li/materials-a

Chrysene-containing polymers functionalized with piperidinium- and quinuclidinium cations, respectively, are prepared by polyhydroxyalkylation and evaluated as anion exchange membranes (AEMs). Experimental results, supported by theoretical considerations, indicate that the chrysene units significantly enhance alkaline stability; a poly(chrysene piperidinium) AEM shows only 16% total ionic loss, compared to 37% for a corresponding poly(terphenyl piperidinium) benchmark after 20 days in 5 M NaOH at 90 °C. Quinuclidinium-functional AEMs show even higher stability with no detectable degradation or ionic loss after the same conditions for 40 days. In addition, the chrysene units promote microphase separation, facilitating hydroxide conductivity, which reaches up to 182 mS cm^{-1} at 80 °C. A selected AEM containing 25% chrysene units is evaluated in a water electrolyzer (AEMWE) single cell with plain Ni foams as electrodes, reaching a current density of 704 mA cm^{-2} at 2.5 V and 90 °C, thereby outperforming a benchmark PiperION® AEM under the same conditions. An *in situ* durability test at 500 mA cm^{-2} for 200 h at 90 °C further confirms the high performance of the AEM. This study demonstrates clear improvements in AEM stability, hydroxide conductivity, and electrolyzer performance achievable by incorporating chrysene units along the polymer backbone.

Introduction

Hydrogen is both a critical feedstock in many industrial processes[1] and an energy carrier with ultra-high energy density, offering a renewable alternative to reduce our reliance on fossil fuels.[2] Currently, hydrogen production predominantly relies on fossil fuel.[3] As the industrial demand for hydrogen continues to grow, the development of cleaner and more sustainable production methods has become increasingly essential to mitigate the environmental impact and support the global objective of achieving net-zero emissions.[4] Green hydrogen, produced *via* water electrolysis using renewable electricity, represents a strategically significant sustainable solution. Among electrolysis technologies, the anion exchange membrane water electrolyzer (AEMWE) has emerged as the most promising one, operating under alkaline conditions with a zero-gap configuration, thereby allowing the use of inexpensive non-noble metal catalysts.[5,6] The AEM is a critical component in AEMWEs, transporting hydroxide ions between the two electrodes and separating the air and hydrogen. The development of high-performance AEMWEs requires AEMs with a comprehensive set of properties, including high hydroxide ion conductivity, robust mechanical strength, and high chemical stability under the harsh alkaline conditions. Over the past two decades, AEMs have been the subject of intensive research, particularly regarding their synthesis and structure–property relationships,[7] and have also been applied in other electrochemical energy conversion and storage systems, such as anion exchange membrane fuel cells (AEMFCs),[8–11] and redox flow batteries.[12,13]

In general, AEMs consist of polymer backbones functionalized with quaternary ammonium cations. Under harsh alkaline conditions, both the polymer backbone and the cations can undergo chemical degradation. For example, AEMs containing aryl ether bonds in the polymer backbone, such as polyethersulfone-based AEMs, generally exhibit poor chemical stability, whereas AEMs with ether-free backbones normally remain stable in alkaline environments.[14] Ether-free poly(arylene piperidinium)s, synthesized *via* superacid-catalyzed polyhydroxyalkylations, show high alkaline stability due to the stable piperidinium cations and were first reported in 2018.[15] Subsequently, poly(arylene piperidinium) AEMs based on different arene monomers have been developed and demonstrated extremely high performance in electrochemical devices.[16–22] However, for long-term operation of electrochemical devices in industrial applications, the demand for AEMs with even higher alkaline stability remains. Recently,

---

Centre for Analysis and Synthesis, Department of Chemistry, Lund University, SE-22100 Lund, Sweden. E-mail: patric.jannasch@chem.lu.se

poly(arylene alkylene) AEMs functionalized with quinuclidinium cations have been reported to possess exceptional alkaline stability.[23,24] This has been attributed to the "cage-like" structure of the bicyclic *N*-methylquinuclidinium cation, efficiently suppressing β-elimination reactions under alkaline conditions.[25]

High-performance AEMs also require high ion conductivity. Different molecular designs of the polymer structure have been extensively investigated to develop synthetic strategies that enhance microphase separation and ionic clustering in AEMs, facilitating the formation of efficiently ion-conducting water-rich channels.[26–28] Recently, the incorporation of fused benzene ring units into polymer backbones of poly(arylene alkylene)s has been shown to significantly improve microphase-separation, resulting in high-performance AEMs.[29,30] The compound chrysene (1,2,5,6-dibenzonaphthalene) consists of four planar fused benzene rings in a "zigzag" arrangement. The extended π-system results in significant electron delocalization, enhancing electronic charge transport and producing a characteristic red–blue fluorescence under UV light. Because of the distinct electronic properties, chrysene and corresponding derivatives have previously been applied in solar cells,[31,32] organic semiconductors,[33,34] and organic transistors.[35]

In the present study, we have successfully prepared poly(arylene piperidinium)s and poly(arylene quinuclidinium)s containing chrysene units *via* superacid-mediated polyhydroxyalkylations involving *p*-terphenyl, chrysene, and either *N*-methylpiperidone or quinuclidone. After quaternization, AEMs with different chrysene contents were cast and investigated concerning, *e.g.*, morphology, water uptake, conductivity, and alkaline stability to investigate the effect of the chrysene units on membrane performance. Furthermore, the AEM with the most favorable *ex situ* properties was selected for evaluation of performance and durability in an AEMWE cell.

Results and discussion

Polymer synthesis and characterization

Chrysene-containing polymers bearing *N*,*N*-dimethylpiperidinium and *N*-methylquinuclidinium cations, respectively, were synthesized in two steps, as shown in Scheme 1 (all materials and experimental methods used are reported in the SI). In the first step, precursor polymers containing *N*-methylpiperidine and quinuclidine groups, respectively, were synthesized by superacid-mediated polyhydroxyalkylations. In both precursor series, the molar feed ratios of chrysene to *p*-terphenyl were adjusted to obtain polymers with different chrysene contents in the backbones. In the sample designations, *x* denotes the molar fraction of chrysene units. Hence, in the piperidine-containing precursor polymers, the chrysene content ranged from 0 to 25, 50, 75, and 100% (*pre*-PCP-*x* with $x = 0, 0.25, 0.50, 0.75$, and 1.0), and for the quinuclidine-containing ones, the chrysene content was set to 25 and 50% (*pre*-PCQ-*x* with $x = 0.25$ and 0.50). Notably, copolymers with a chrysene content exceeding 50% were found to form very brittle materials.

During the polymerizations involving *N*-methyl-4-piperidone, the viscosity of the polymerization solutions increased rapidly, which likely indicated a high reactivity of chrysene with the piperidone. In comparison, polymerizations involving 3-quinuclidone required longer reaction times, despite the use of a higher temperature and concentration, suggesting a comparatively lower reactivity of the quinuclidone compared to *N*-methyl-4-piperidone. The structure of the precursor polymers was characterized by ^{1}H NMR spectroscopy, and the spectra of the *pre*-PCP-*x* and *pre*-PCQ-*x* samples recorded in DMSO-d_6 with the addition of 5 vol% TFA are displayed in Fig. S3–S7. The signal at around 9.5 ppm in the spectra of the precursor polymers originated from the protonated tertiary piperidine and tertiary quinuclidine groups, respectively. In the second step, the amine groups of the precursor polymers were quaternized in Menshutkin reactions with methyl iodide. The spectra of the quaternized PCP-*x* and PCQ-*x* polymers, recorded in DMSO-d_6 after the addition of 5 vol% TFA, are shown in Fig. 1, S8, and S9. The complete disappearance of the signals of the protonated tertiary piperidine and tertiary quinuclidine groups, respectively, confirmed the quantitative quaternizations.

The quaternized PTP, PCP-*x*, and PCQ-*x* polymers were dissolved in DMSO and cast into AEMs in a ventilated oven at 80 °C. Notably, the homopolymer PCP-1.0, exclusively containing chrysene units, formed a robust and flexible membrane. To the best of our knowledge, this is the first reported case in which a homopolymer based on a fully fused benzene ring monomer and piperidone has formed a mechanically strong membrane. This may be the result of the high reactivity between chrysene and piperidone in the polyhydroxyalkylation. After casting, the AEMs were ion-exchanged to the bromide form and titrated to determine the ion exchange capacity (IEC). The experimental IEC values of the AEMs closely matched the theoretical values, providing further evidence of complete quaternization reactions (Table 1). Because chrysene and *p*-terphenyl have very similar molecular weights (228.28 g mol^{-1} and 230.30 g mol^{-1}, respectively), all the AEMs showed similar IEC values (IEC$_{\mathrm{Br-}}$ ranging from 2.34 to 2.41 mequiv mol^{-1}) regardless of monomer content. Unfortunately, determining the contents of aromatic copolymers is notoriously difficult because of the often broad and overlapping proton signals in the aromatic region. In the present case, the signals of the *p*-terphenyl and chrysene units were sufficiently overlapped to disable a meaningful compositional determination (Fig. S1 and S2). The chrysene signals appeared between 7.5 and 9.3 ppm, while the ones from the *p*-terphenyl units were observed in a more narrow range between 7.3 and 7.7 ppm. However, the trends in the ^{1}H NMR spectra indicated that the copolymer content closely followed the feed ratio of the aromatic monomers in the polymerizations.

Intrinsic viscosity measurements were performed to estimate the molecular weights of the PTP, PCP-*x*, and PCQ-*x* polymers, and the results are summarized in Table 1. The measurements were carried out with the polymers dissolved in 0.1 M LiBr solution in DMSO to suppress the polyelectrolyte effect (notably, the intrinsic decreases with the salt

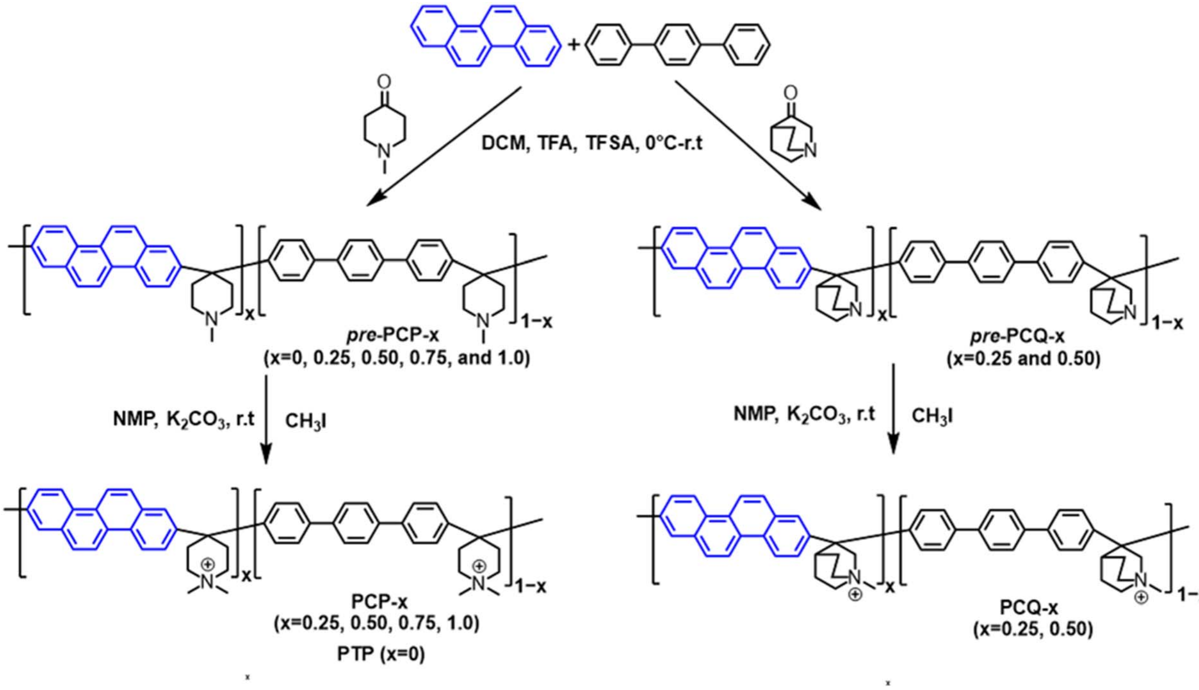

Scheme 1 Synthetic pathways to chrysene-containing polymers functionalized with piperidinium and quinuclidinium cations, respectively, *via* polyhydroxyalkylation and quaternization.

concentration). In the piperidinium-containing series, all polymers showed medium to high intrinsic viscosity values, ranging from 0.34 to 0.56 dL g^{-1}. An increase in the chrysene content was found to decrease the intrinsic viscosity of the respective polymers. The values of the quinuclidinium-containing PCQ-*x* polymers (0.21–0.25 dL g^{-1}) were lower than for corresponding piperidinium-containing samples with the same chrysene content, which may indicate a lower reactivity of 3-quinuclidone, compared with *N*-methyl-4-piperidone, in the polyhydroxyalkylations.

Water uptake and swelling

The water uptake data of the AEMs are shown in Fig. 2c and Table 1. Because all the AEMs have high $\mathrm{IEC}_{\mathrm{OH}^-}$ values (2.75–2.84 mequiv mol^{-1}), the water uptake of all AEMs was above 100% at 20 °C. For the piperidinium-functionalized AEMs, the water uptake increased with increasing chrysene content. For example, the water uptake rose from 265% for the PTP membrane (0% chrysene content) to 608% for the PCP-0.75 membrane (75% chrysene content) at 80 °C. The data of PCP-1.0 was not evaluated at 80 °C because of the extremely high uptake, which led to severe swelling and mechanical fragility, making accurate measurements difficult. The increase in water uptake of the AEMs in PCP-*x* series with the chrysene content may be a combination of a decrease in the molecular weight of the polymers and an increase in free volume with increasing chrysene content, while the increase in water uptake in PCQ-*x* AEMs with increasing chrysene content was more possibly due to the latter reason. An increase in free volume in AEMs containing fused benzene ring units has recently been reported.[36] The water uptake of the quinuclidinium-functionalized PCQ-*x*

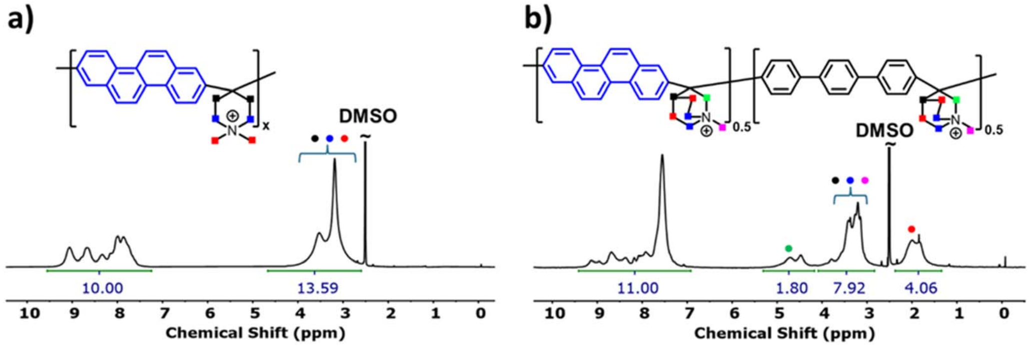

Fig. 1 Representative ^{1}H NMR spectra of the quaternized polymers: (a) PCP-1.0 and (b) PCQ-0.50 recorded in DMSO-d_6 with 5 vol% TFA.

Table 1 Data of the chrysene-containing AEMs

	IEC (mequiv g^{-1})				σ (mS cm^{-1})				
AEM	Theoretical[a]	Titrate	WU (%) 20 °C	WU (%) 80 °C	20 °C	80 °C	λ (80 °C)	$T_{d,95}$ (°C)	$[\eta]$ (dL g^{-1})
PTP	2.38 (2.80)	2.41 (2.84)	106	265	70	139	52	289	0.56
PCP-0.25	2.38 (2.80)	2.39 (2.81)	124	420	82	175	83	320	0.52
PCP-0.50	2.38 (2.80)	2.42 (2.86)	121	515	76	178	102	309	0.43
PCP-0.75	2.39 (2.81)	2.40 (2.83)	126	608	74	160	120	309	0.38
PCP-1.0	2.39 (2.81)	2.43 (2.87)	153	n.e	68	144	n.e	341	0.34
PCQ-0.25	2.32 (2.72)	2.35 (2.76)	110	309	77	182	61	351	0.21
PCQ-0.50	2.32 (2.72)	2.34 (2.75)	113	325	60	142	64	365	0.25

[a] Calculated from polymer structures in the Br^- form (OH^- form within parentheses). *n.e: not evaluated because of excessive uptake.

membranes was lower compared to the piperidinium-functionalized PCP-*x* membranes, and the swelling of the AEMs increased with the water uptake (Fig. 2d and e). Notably, the PCQ-0.25 and PCQ-0.50 membranes maintained an in- and through-plane swelling equal to, or below, 50% at 80 °C.

The uptake and swelling of the present AEMs and the commercial PiperION® 60 membrane in 2 M KOH (aq.) solution are reported in Fig. S11. As expected, compared with the water uptake, the uptake of the KOH solution by the AEMs was significantly lower. For example, the alkaline uptake of PCP-1.0 was approximately 130% at 80 °C, compared to the water uptake of this membrane, which exceeded 400% at 60 °C.

Morphology and mechanical properties

Atomic force microscopy (AFM) was employed to analyze the surfaces of dry AEM samples in the bromide form to study the impact of the chrysene content on membrane morphology (Fig. 3). For the piperidinium-functionalized AEM samples, the PTP sample (0% chrysene) showed no clear hydrophilic (dark)–hydrophobic (bright) phase separation. Increasing the chrysene content to 25% clearly promoted the microphase separation in the PCP-0.25 sample. Further increases in chrysene content made the hydrophobic phase more dominant and distinct in the PCP-1.0 sample. Still, the hydrophilic phase domain remained well-distributed and continuous. The hydrophilic channel width and area fraction of the AEMs are reported in Fig. S12. The hydrophilic area fraction increased significantly from PTP (25%) to PCP-0.25 (46%) and PCP-0.50 (45.1%), but decreased in PCP-1.0 (40%). In the quinuclidinium-functional membrane series, the PCQ-0.25 sample exhibited a distinctly microphase-separated morphology with a regular and continuous hydrophilic phase domain. The hydrophilic area fraction of PCQ-0.25 was larger than that of PCQ-0.50 (Fig. S12). The AFM data indicated that an increased chrysene content enhanced microphase separation and the formation of a morphology with an increasing size of the hydrophobic phase domain. This suggests that the chrysene content should be optimized to achieve a morphology with a balanced content of hydrophilic-hydrophobic phase domains.

Small-angle X-ray scattering (SAXS) was used to study the bulk morphology of the dry AEMs in the bromide form. However, no distinct ionomer peak was observed in the SAXS profiles for any of the AEM samples (Fig. S13). This may be due to the highly rigid chrysene-containing polymer backbones and the limited local mobility of the piperidinium and quinuclidinium cations tethered to the polymer backbones, limiting ionic clustering during the membrane casting process.

The mechanical properties of dry and wet AEMs were evaluated by tensile testing, and the results are shown in Fig. 4, S14, and S15. In the dry state, the AEMs exhibited high tensile strength, with a strength at break reaching 53.7 MPa, displaying a 0.5% secant modulus up to 1900 MPa (Fig. 4a and S15). The mechanical strength of the dry samples was strongly correlated with the molecular weight of the polymers, as the tensile strength at break decreased from 53.7 MPa for the PTP sample ($[\eta] = 0.56$ dL g^{-1}) to 20.6 MPa for the PCP-1.0 sample ($[\eta] = 0.34$ dL g^{-1}). In the wet state (Fig. 4b and S13), the tensile strength was, as expected, lower than in the dry state but still reached up to 20 MPa, with the strain at break exceeding 40%. Based on this data, the AEMs had sufficient mechanical properties for electrochemical device testing.

Hydroxide conductivity

Hydroxide conductivity is a key parameter of AEMs that directly determines the performance in electrochemical devices. In the present work, the incorporation of chrysene into the AEM polymer backbones improved the hydroxide conductivity of the membranes (Fig. 2a). For the piperidinium-functionalized AEMs, an increasing chrysene content raised the hydroxide conductivity from 139 mS cm^{-1} (PTP, 0% chrysene) to 175 mS cm^{-1} (PCP-0.25) and 178 mS cm^{-1} (PCP-0.50) at 80 °C. When the chrysene content exceeded 50%, the hydroxide conductivity began to decrease, most likely because of the change in morphology discussed above, and the high water content causing a dilution effect.[37] In the quinuclidinium series, PCQ-0.25 (25% chrysene) reached a hydroxide conductivity of 182 mS cm^{-1}, which dropped to 142 mS cm^{-1} for PCQ-0.50 (50% chrysene) at 80 °C (Fig. 2b). This difference can be explained by the more distinct microphase separation observed in PCQ-0.25, as discussed in morphology and mechanical properties section.

Fig. 2f shows the hydroxide conductivity of the AEMs as a function of the hydration number. Membrane PCQ-0.25 displayed the highest hydroxide conductivity at the lowest

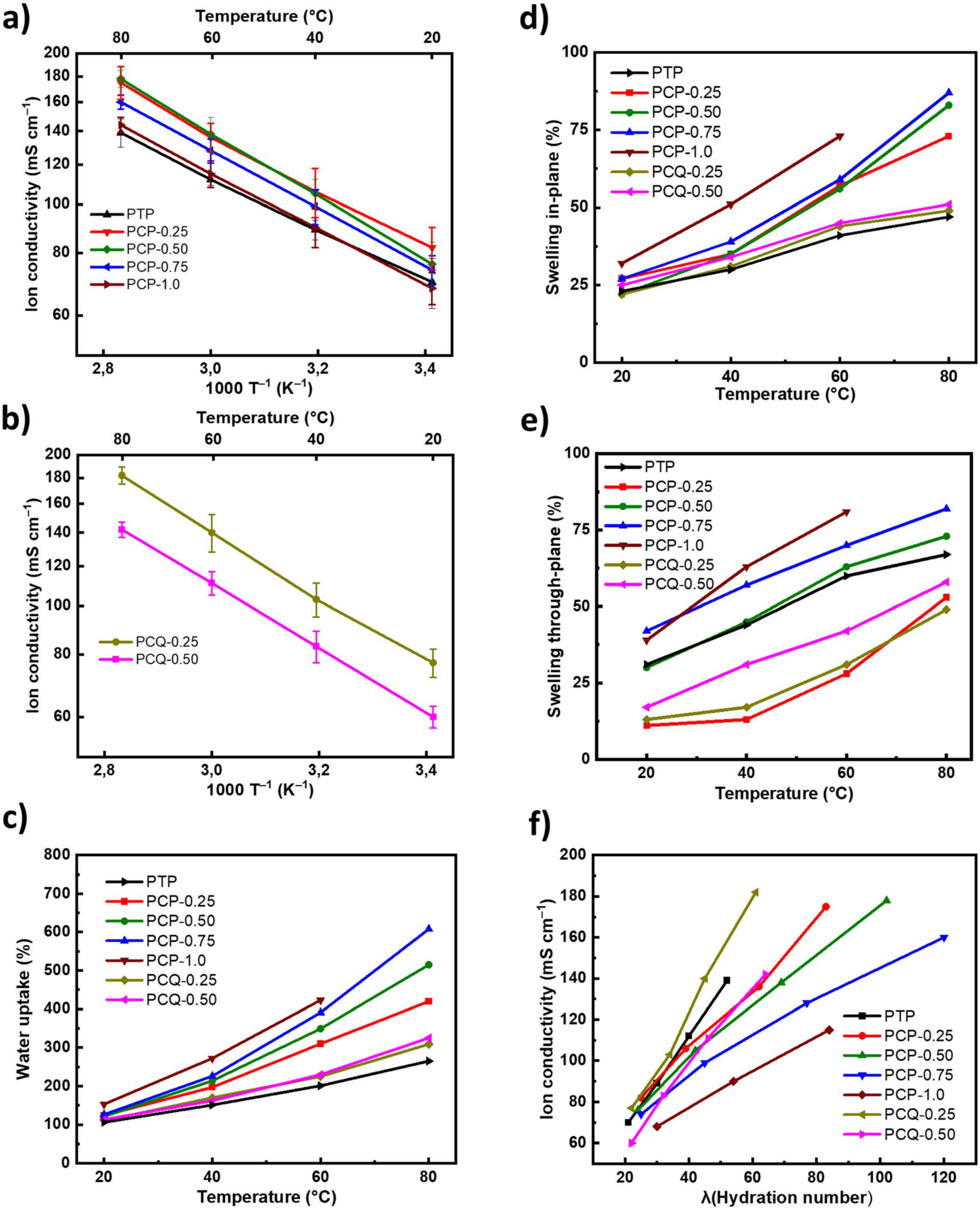

Fig. 2 Water uptake, swelling, and conductivity of the AEMs: (a) hydroxide conductivity of the piperidinium-functionalized series, (b) hydroxide conductivity of the quinuclidinium-functionalized series, (c) water uptake of all the AEMs, (d) in-plane swelling, (e) through-plane swelling, and (f) hydroxide conductivity as a function of hydration number ($\lambda = [H_2O]/[\text{cation}]$). All the data were measured with fully hydrated (immersed) AEMs.

hydration level, indicating superior efficiency in the use of the water for hydroxide ion transport. In the PCP-*x* series, the slope of the graph became significantly less steep from PCP-0.50 to PCP-0.75, indicating a negative effect of excessive water uptake on the conductivity (Fig. 2f). Overall, these results demonstrate

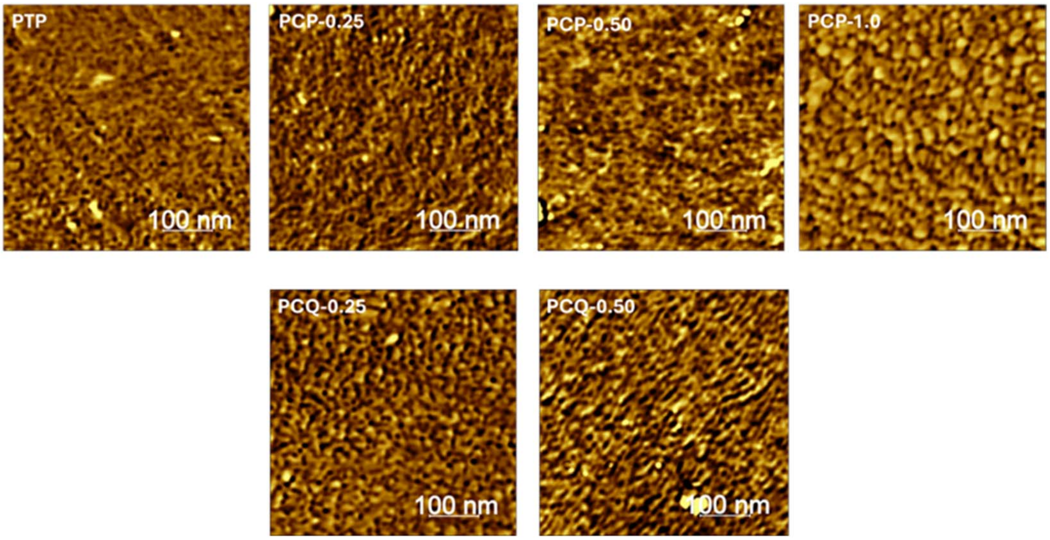

Fig. 3 AFM phase images of the dried AEMs in bromide form.

that incorporating an optimized content of chrysene improves the hydroxide conductivity of AEMs.

Alkaline and thermal stability

Alkaline stability is a critical property of AEMs, demonstrating their ability to retain molecular structure and function in a highly alkaline environment. The *ex situ* alkaline stability of the AEMs was evaluated by immersing membrane samples in 2 and 5 M NaOH (aq.) during specific periods. ^{1}H NMR spectroscopy of membrane samples, dissolved in DMSO-d_6 with 5 vol% TFA, before and after storage revealed any structural changes (Fig. 5a–e). Some of the signals at around 8 ppm and below 2 ppm resulted from the added TFA and were also observed in the ^{1}H NMR spectrum of neat TFA in DMSO-d_6 (Fig. S10). In the series of piperidinium-functionalized AEMs, PTP, PCP-0.50, and PCP-1.0 were selected for the alkaline stability evaluation (Fig. 5a–c). The common degradation pathways and products of the *N*,*N*-dimethylpiperidinium cation under hydroxide attacks are displayed in Fig. 5f. New signals appearing after the alkaline storage at around 5 ppm and 6.5 ppm originated from vinylic groups formed by β-elimination of piperidinium cations, leading to ionic loss and the formation of tertiary amines (Fig. 5f). The new signal at around 9.5 ppm and 8.4 ppm originated from (protonated) amines formed in elimination (and possibly substitution) reaction products, respectively, and was used to quantify the total ionic loss. Notably, the AEMs became more stable with increasing chrysene contents under the employed conditions. PCP-1.0 showed no detectable degradation after storage for 20 days in 2 M NaOH at 90 °C (Fig. 5c), and PCP-0.50 showed negligible degradation that was difficult to quantify (Fig. 5b), while PTP clearly degraded, with new signals appearing to indicate a 7% total ionic loss (Fig. 5a).

Under harsher alkaline conditions, the differences in alkaline stability among AEMs with different chrysene contents became more significant. The total ionic losses of PTP, PCP-0.50, and PCP-1.0 were 37, 25, and 16%, respectively, after 20

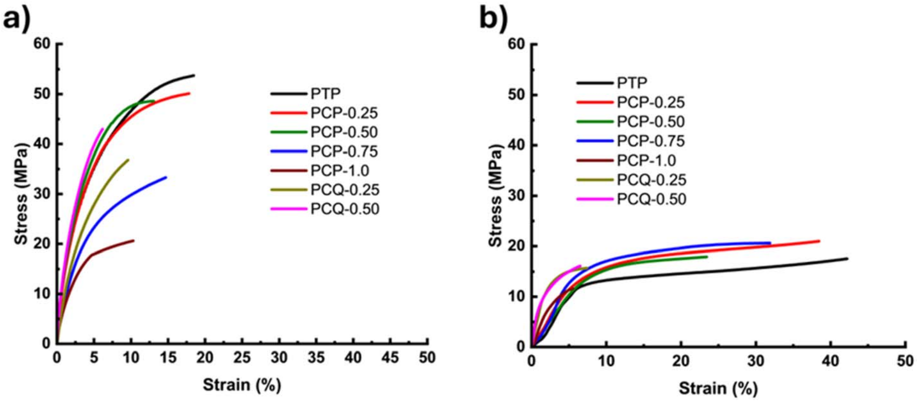

Fig. 4 Stress–strain data of the PCP-*x* and PCQ-*x* AEMs in the bromide form, recorded in the (a) dry and (b) wet state at 30 °C during a 0.5 N min^{-1} ramping force test.

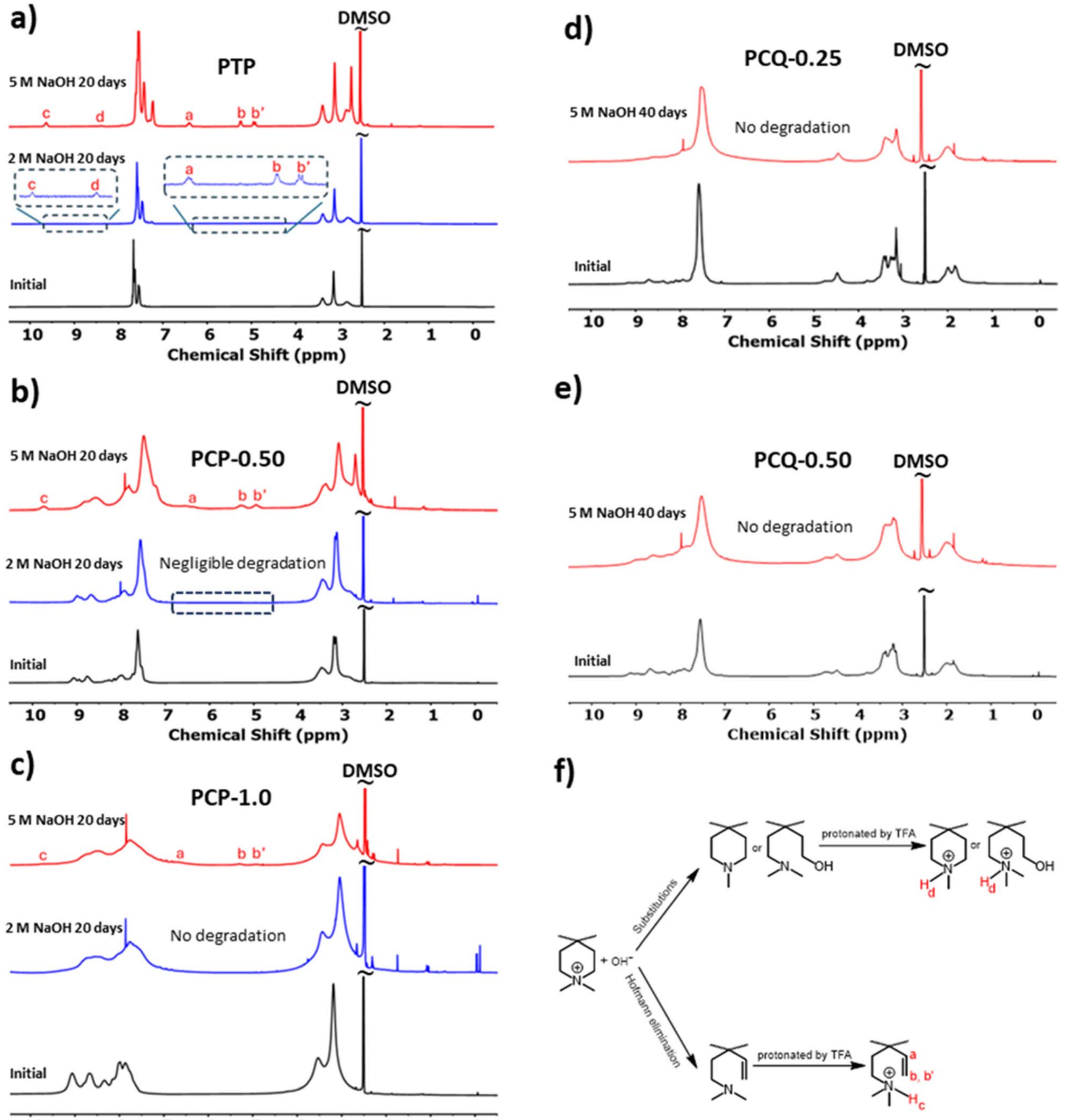

Fig. 5 ^{1}H NMR spectra of (a) PTP, (b) PCP-0.50, (c) PCP-1.0, (d) PCQ-0.25, (e) PCQ-0.50 AEMs before and after 20- and 40 days storage, respectively, in 2 and 5 M NaOH at 90 °C, and (f) an outline of common degradation pathways and products of *N*,*N*-dimethylpiperidinium cation under hydroxide attacks (including ^{1}H NMR signal designations after protonation by TFA).

days in 5 M NaOH at 90 °C. A 57% decrease in total ionic loss was observed when comparing PTP (0% chrysene) with PCP-1.0 (100% chrysene). Motivated by this significant finding, quantum chemical calculations were carried out to study the electron density distributions in three different 4,4-diaryl-*N*,*N*-dimethylpiperidinium model compounds (Fig. S16). Electrostatic potential (ESP) maps (Fig. S16) showed differences in the maximum ESP values at the N atoms of the *N*,*N*-dimethylpiperidinium cations of the three model compounds. A higher ESP value at the N atom in the dimethyl piperidinium cation implies a higher tendency for nucleophilic attack by hydroxide ions.[38] The ESP analysis showed that the model compound with two chrysene substituents at the 4-position of the *N*,*N*-dimethylpiperidinium cation had the lowest maximum ESP value (4.684 eV), followed by the model compound with one chrysene and one *p*-terphenyl substituent (4.692 eV). The model compound with two *p*-terphenyl substituents had the highest maximum ESP value (4.715 eV). This observation indicated the benefit of the planar conjugated chrysene structure to improve the alkaline stability of the AEMs, as planarity facilitates electron delocalization, thereby enhancing the electron density of the piperidinium cation and mitigating nucleophilic attacks by hydroxide ions. The combination of the experimental observations and the computational results strongly supported that the incorporation of chrysene units into the polymer backbone significantly improves the alkaline stability of the AEMs. In addition, the increase in water uptake with increasing chrysene content may slightly contribute to improving alkaline stability in piperidinium-functionalized AEMs. In the series of quinuclidinium-functional AEMs, the PCQ-0.25 and PCQ-0.50 samples exhibited exceptional stability, showing no structural degradation after 40 days in 5 M NaOH at 90 °C, which is attributed to the highly robust 'cage-like' structure of the *N*-methylquinuclidinium cation and the proximity of the chrysene units.

The thermal stability of the AEMs in the bromide form was studied by TGA, and the results are shown in Fig. 6 and Table 1. No AEM exhibited any thermal decomposition below 230 °C. Among piperidinium-functionalized AEMs, PTP (0% chrysene) had the lowest thermal decomposition temperature with $T_{d,95}$ = 289 °C, while the $T_{d,95}$ values of the chrysene-containing samples PCP-0.25, PCP-0.50, PCP-0.75, and PCP-1.0 were all above 308 °C (Table 1). In comparison, the thermal stability of the quinuclidinium-functionalized AEMs was higher than that of the piperidinium-functionalized AEMs, with $T_{d,95}$ values exceeding 350 °C for all samples. A higher thermal stability of quinuclidininum-functionalized AEMs, compared to piperidinium ones, has been reported previously.[39]

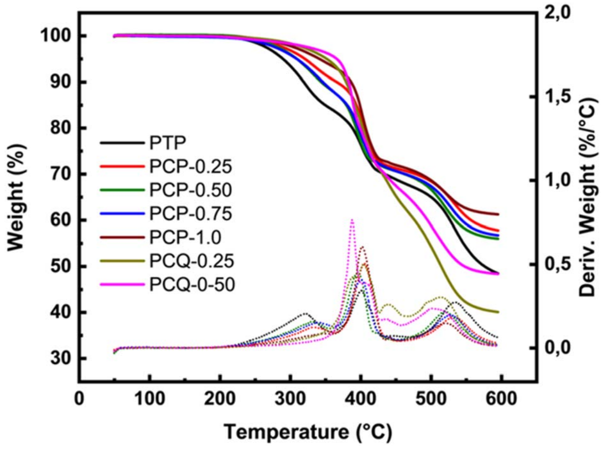

Fig. 6 TGA traces corresponding derivative weight data of the AEMs recorded under N_2 atmosphere at a heating rate of 10 °C min^{-1}.

AEMWE performance and durability evaluations

In the present study, AEMWE operation was conducted to evaluate the initial feasibility and operational stability of the synthesized membrane, with electrochemical characterizations focused on device-level performance rather than in-depth mechanistic investigation. The components and structure of the 6.25 cm^2 AEMWE test cell are shown in Scheme S1. Based on the high hydroxide conductivity and excellent alkaline stability of PCQ-0.25, a 65 μm-thick sample of this membrane was selected for a detailed AEMWE evaluation. Plain uncatalyzed nickel foams (*i.e.*, completely non-platinum) were used as electrode layers, and a 2 M KOH (aq.) solution was employed as the electrolyte. Although Ni foam is not a high-performance catalyst material for AEMWE, this material was chosen in the present study because of its low cost, accessibility, and well-established tolerance to high electrolyte concentrations. These features allow Ni foam to serve as a benchmark catalyst, enabling comparisons of membrane performance across different AEMWE setups and research groups. The polarization curves were obtained from Staircase Galvanostatic Electrochemical Impedance Spectroscopy (SGEIS) measurements, as described in SI, Section 1.17. As the operational temperature of the AEMWE single cell was raised from 70 to 80 and 90 °C, the current density successively increased from 545 to 592 and 704 mA cm^{-2}, respectively, at a potential of 2.5 V (Fig. 7b). The expected improvement in cell performance with increasing temperature was attributed to enhanced electrode kinetics and the hydroxide conductivity of the PCQ-0.25 AEM. As a benchmark, a 60 μm-thick commercial PiperION® AEM was evaluated under the same conditions as the PCQ-0.25 AEM. The properties of PiperION® AEM was reported in SI Table S1. The results showed that the PCQ-0.25-based cell (704 mA cm^{-2} at 2.5 V) achieved a higher performance than the PiperION®-based cell (656 mA cm^{-2} at 2.5 V) at 90 °C (Fig. 7a). The higher performance of the former cell was attributed to the high hydroxide conductivity of the PCQ-0.25 AEM (182 mS cm^{-1} at 80 °C in pure water). Subsequent studies by electrochemical impedance spectroscopy (EIS) to examine the influence of the AEMs on AEMWE performance furthermore confirmed the advantage of the PCQ-0.25 AEM, and the cell assembled with PCQ-0.25 exhibited a lower ohmic resistance (0.080 Ω) compared to that with PiperION® 60 (0.091 Ω) (Fig. 7d).

The *in situ* stability of the PCQ-0.25-based cell was evaluated at a constant current density of 500 mA cm^{-2} during 200 h at 90 °C, with the 2 M KOH electrolyte refreshed every 25 h (Fig. 7e). During the first 25 h period of operation, the voltage increased to 2.47 V but began to decrease in the subsequent 25 h period. At the end of each period, the voltage ranged from 2.36 to 2.44 V. Because the cell voltage required time to reach a stable value after each period, the first 5 h of each period was excluded in the linear fitting used to calculate the voltage decay. After the 200 h durability test, the cell showed some degradation, with a voltage decay rate of 0.237 mV h^{-1}. A comparison of the polarization curves before and after the durability evaluation revealed that the current density at 2.5 V decreased from 704 mA cm^{-2} (before test) to 640 mA cm^{-2} (after test) (Fig. 7c).

The chemical structure of the PCQ-0.25 AEM before and after the durability test was characterized by ^{1}H NMR spectroscopy to detect any changes in molecular structure. Although the AEMWE test conditions were extreme, *i.e.*, operating at 90 °C while maintaining a cell voltage above 2.3 V for most of the operation, the chemical structure of the PCQ-0.25 AEM showed

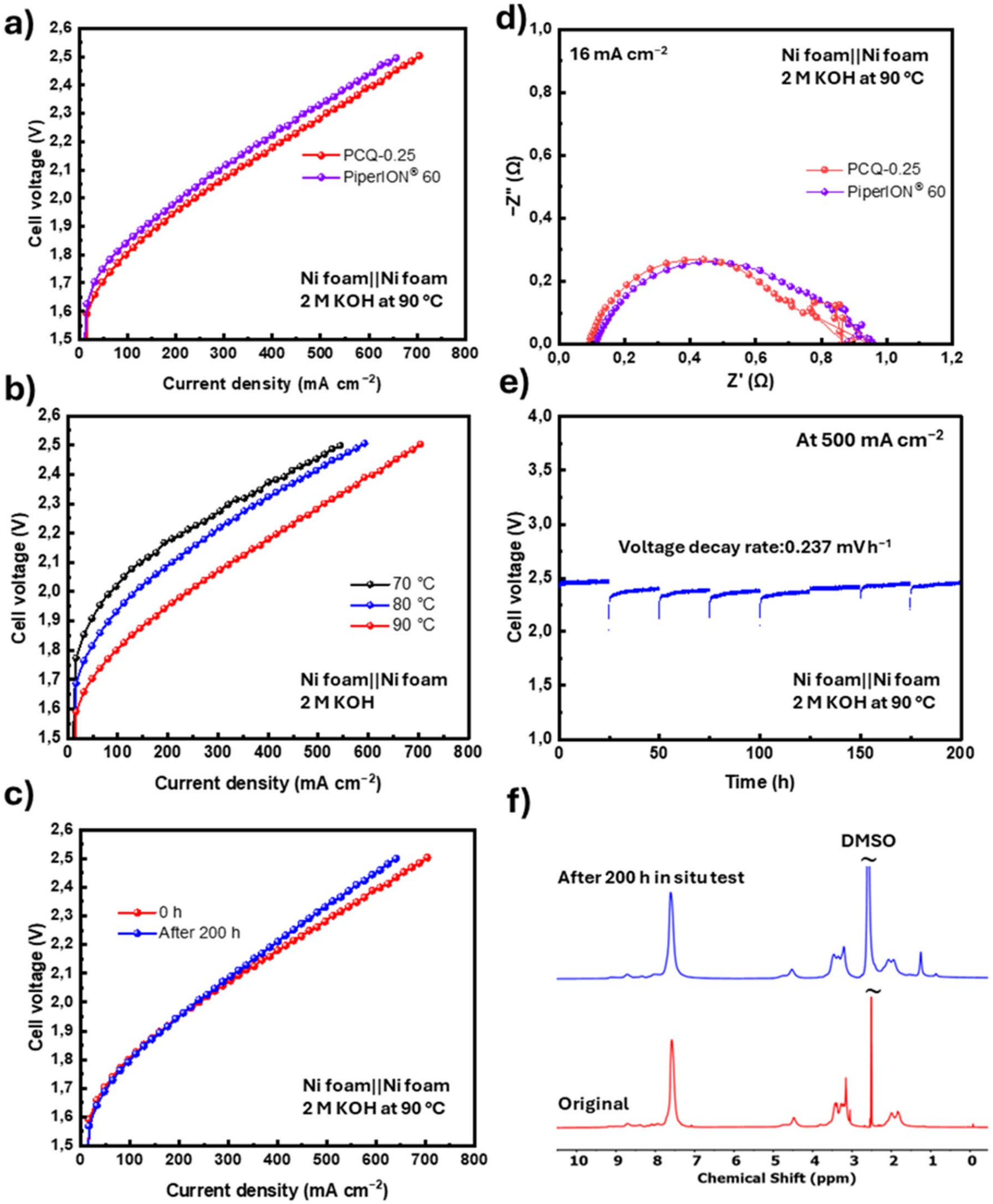

Fig. 7 *I–V* curves of AEMWE cells assembled with: (a) PiperION® 60 and PCQ-0.25 in 2 M KOH at 90 °C, (b) PCQ-0.25 in 2 M KOH at different temperatures, (c) PCQ-0.25 in 2 M KOH at 90 °C recorded before and after 200 h *in situ* stability test at 500 mA cm^{-2}, and (d) electrochemical impedance spectroscopy (EIS) spectra of the PiperION® 60 and PCQ-0.25 membranes at 90 °C, (e) *in situ* stability test of PCQ-0.25 for 200 h at 500 mA cm^{-2} and 90 °C, and (f) ^{1}H NMR spectra of PCQ-0.25 before and after the *in situ* stability test.

no detectable degradation after the evaluation (Fig. 7f), demonstrating a superior alkaline stability of the quinuclidinium-functionalized PCQ-0.25 AEM. This suggested that the observed degradation in AEMWE performance may originate from the electrodes. EIS analysis of the PCQ-0.25-based cell before and after the durability test showed that the ohmic resistance had increased from 0.080 to 0.088 Ω, while the charge transfer resistance increased from 0.753 to 0.824 Ω (Fig. S17). The reason may be that during long-term high-voltage operation in the alkaline solution, when the single test cell operated above 2.3 V during the durability test in 2 M KOH, the Ni foams underwent *in situ* electrochemical oxidation to form NiOOH.[40] Although NiOOH is well known for its high oxygen evolution reaction (OER) activity, a recent study has shown that a thick NiOOH layer can form on Ni foam surfaces under high potential in KOH solution.[41] This thick layer can negatively affect AEMWE performance by increasing the ohmic resistance, or making it more difficult for oxygen to escape from the electrode surface. Another contributing factor to the performance decrease may be corrosion of the cell hardware.[42]

The AEMWE and durability evaluations demonstrated the exceptional properties of the PCQ-0.25 AEM and its promising application potential, thus motivating further studies of chrysene-containing AEMs in combination with improved catalyst systems to further boost AEMWE performance.

Conclusions

Two series of anion exchange polymers with different chrysene contents, functionalized with piperidinium and quinuclidinium cations, respectively, were successfully prepared by polyhydroxyalkylations. The polymers formed mechanically strong AEMs, and the incorporation of chrysene induced distinct microphase-separated morphologies which enabled a high hydroxide conductivity, reaching up to 180 mS cm^{-1} at 80 °C. In addition, in the piperidinium-functionalized series of AEMs, the incorporation of chrysene into the polymer structure significantly enhanced the alkaline stability. The quinuclidinium-functionalized AEMs containing chrysene showed exceptional alkaline stability, with no degradation was observed after 40 days in 5 M NaOH at 90 °C. A quinuclidinium-functionalized AEM containing 25% chrysene units demonstrated a very high performance in the AEMWE evaluation, achieving higher performance than a commercial benchmark membrane. Furthermore, the former AEM showed no structural degradation after a 200 h durability test at 90 °C in the AEMWE cell. Overall, the results of the present study demonstrated the advantageous effects on AEM performance by incorporating fused benzene ring structures such as chrysene into polymer backbones, providing an effective strategy for developing high-performance AEMs for alkaline electrolyzers and fuel cells.

Author contributions

Triet Nguyen Dai Luong: conceptualization, methodology, investigation, validation, writing – original draft. Patric Jannasch: methodology, funding acquisition, supervision, writing – review & editing.

Conflicts of interest

There are no conflicts to declare.

Data availability

The data supporting this article have been included as part of the supplementary information (SI). Supplementary information: detailed descriptions of materials and experimental methods, ^{1}H NMR spectra of the polymers, alkaline uptake and swelling data, SAXS profiles, stress-strain data, and electrostatic potentials diagrams of chrysene-containing model compounds. See DOI: https://doi.org/10.1039/d5ta10393b.

Acknowledgements

This work was supported by the Swedish Foundation for Strategic Research (SSF) through the "PUSH" project (grant ARC19-0026), the Swedish Energy Agency (grants 50519-1, 45057-1, 37806-3 and 45515-3), the Swedish Research Council (grant 2023-04525), and the Royal Physiographic Society in Lund. We thank Peter Holmqvist for assistance with the SAXS measurement, and Anders Sundin for assistance with the computational work.

References

1 N. Rambhujun, M. S. Salman, T. Wang, C. Pratthana, P. Sapkota, M. Costalin, Q. Lai and K.-F. Aguey-Zinsou, *MRS Energy Sustain.*, 2020, **7**, 33.

2 M. Chatenet, B. G. Pollet, D. R. Dekel, F. Dionigi, J. Deseure, P. Millet, R. D. Braatz, M. Z. Bazant, M. Eikerling, I. Staffell, P. Balcombe, Y. Shao-Horn and H. Schäfer, *Chem. Soc. Rev.*, 2022, **51**, 4583–4762.

3 M. Davis, A. Okunlola, G. Di Lullo, T. Giwa and A. Kumar, *Renewable Sustainable Energy Rev.*, 2023, **171**, 112962.

4 P. J. Megía, A. J. Vizcaíno, J. A. Calles and A. Carrero, *Energy Fuels*, 2021, **35**, 16403–16415.

5 L. Wan, Z. Xu, Q. Xu, M. Pang, D. Lin, J. Liu and B. Wang, *Energy Environ. Sci.*, 2023, **16**, 1384–1430.

6 D. Li, A. R. Motz, C. Bae, C. Fujimoto, G. Yang, F.-Y. Zhang, K. E. Ayers and Y. S. Kim, *Energy Environ. Sci.*, 2021, **14**, 3393–3419.

7 W. You, K. J. T. Noonan and G. W. Coates, *Prog. Polym. Sci.*, 2020, **100**, 101177.

8 C. Yang, L. Liu, X. Han, Z. Huang, J. Dong and N. Li, *J. Mater. Chem. A*, 2017, **5**, 10301–10310.

9 L. Wang, M. Bellini, H. A. Miller and J. R. Varcoe, *J. Mater. Chem. A*, 2018, **6**, 15404–15412.

10 A. G. Wright, J. Fan, B. Britton, T. Weissbach, H.-F. Lee, E. A. Kitching, T. J. Peckham and S. Holdcroft, *Energy Environ. Sci.*, 2016, **9**, 2130–2142.

11 M. S. Cha, J. E. Park, S. Kim, S.-H. Han, S.-H. Shin, S. H. Yang, T.-H. Kim, D. M. Yu, S. So, Y. T. Hong, S. J. Yoon, S.-G. Oh, S. Y. Kang, O.-H. Kim, H. S. Park, B. Bae, Y.-E. Sung, Y.-H. Cho and J. Y. Lee, *Energy Environ. Sci.*, 2020, **13**, 3633–3645.

12 M. Arunachalam, A. Sinopoli, F. Aidoudi, S. E. Creager, R. Smith, B. Merzougui and B. Aïssa, *ACS Appl. Mater. Interfaces*, 2021, **13**, 45935–45943.

13 I. Salmeron-Sanchez, P. Mansouri Bakvand, A. Shirole, J. Ramón Avilés-Moreno, P. Ocón, P. Jannasch, R. Wreland Lindström and A. Khataee, *Chem. Eng. J.*, 2023, **474**, 145879.

14 A. D. Mohanty, S. E. Tignor, J. A. Krause, Y.-K. Choe and C. Bae, *Macromolecules*, 2016, **49**, 3361–3372.

15 J. S. Olsson, T. H. Pham and P. Jannasch, *Adv. Funct. Mater.*, 2018, **28**, 1702758.

16 G. W. Ryoo, S. Shin, I. W. Song, J. Lim, H. Shin, K. C. Kwon, S. H. Park, J. Y. Lee and M. S. Kwon, *Adv. Funct. Mater.*, 2024, **34**, 2408545.

17 W. Song, K. Peng, W. Xu, X. Liu, H. Zhang, X. Liang, B. Ye, H. Zhang, Z. Yang, L. Wu, X. Ge and T. Xu, *Nat. Commun.*, 2023, **14**, 2732.

18 H. Zhang, W. Xu, W. Song, K. Peng, L. Sun, C. Yang, X. Zhang, H. Zhang, B. Ye, X. Liang, Z. Yang, L. Wu, X. Ge and T. Xu, *Nat Sustainability*, 2024, **7**, 910–919.

19 N. Chen, S. Y. Paek, J. Y. Lee, J. H. Park, S. Y. Lee and Y. M. Lee, *Energy Environ. Sci.*, 2021, **14**, 6338–6348.

20 N. Chen, H. H. Wang, S. P. Kim, H. M. Kim, W. H. Lee, C. Hu, J. Y. Bae, E. S. Sim, Y.-C. Chung, J.-H. Jang, S. J. Yoo, Y. Zhuang and Y. M. Lee, *Nat. Commun.*, 2021, **12**, 2367.

21 Z. Li, S. Lu, L. Gao, X. Ruan, X. Jiang, X. Yan and G. He, *Adv. Funct. Mater.*, 2025, 2511710.

22 N. Chen, C. Hu, H. H. Wang, S. P. Kim, H. M. Kim, W. H. Lee, J. Y. Bae, J. H. Park and Y. M. Lee, *Angew. Chem., Int. Ed.*, 2021, **60**, 7710–7718.

23 M. Zeng, X. He, J. Wen, G. Zhang, H. Zhang, H. Feng, Y. Qian and M. Li, *Adv. Mater.*, 2023, **35**, 2306675.

24 H. Zhang, X. He, H. Feng, C. Li and M. Li, *J. Mater. Chem. A*, 2024, **12**, 23570–23576.

25 L. Yin, R. Ren, L. He, W. Zheng, Y. Guo, L. Wang, H. Lee, J. Du, Z. Li, T. Tang, G. Ding and L. Sun, *Angew. Chem.*, 2024, **136**, e202400764.

26 F. Zhang, Y. Zhang, L. Sun, C. Wei, H. Zhang, L. Wu, X. Ge and T. Xu, *Angew. Chem., Int. Ed.*, 2023, **62**, e202215017.

27 A. H. N. Rao, S. Nam and T.-H. Kim, *J. Mater. Chem. A*, 2015, **3**, 8571–8580.

28 X. Wu, N. Chen, C. Hu, H. Klok, Y. M. Lee and X. Hu, *Adv. Mater.*, 2023, **35**, 2210432.

29 C. Wei, W. Yu, Y. Zhang, F. Zhang, M. Li, X. Shen, K. Zhang, X. Ge, L. Wu and T. Xu, *J. Power Sources*, 2023, **553**, 232247.

30 T. N. Dai Luong, S. Chen and P. Jannasch, *J. Membr. Sci.*, 2025, **719**, 123724.

31 Z. Tang, T. Li, Y. Cao, Y. Zhang, L. He, A. Zheng and M. Lei, *ChemSusChem*, 2021, **14**, 4923–4928.

32 X. Zhang, S. Zhang, X. Liao, B. Ding, G. Rahim, K. Zhao, J. Chen, M. Han, Y. Zhou, P. Shi, K. Zhang, S. Kinge, H. Zhang, R. Wang, K. G. Brooks, S. Dai, X. Liu, Z. Fei, P. J. Dyson, M. K. Nazeeruddin and Y. Ding, *Adv. Funct. Mater.*, 2024, **34**, 2314086.

33 R. Khatua, S. R. Sahoo, S. Sharma, R. Thangavel and S. Sahu, *J. Phys. Org. Chem.*, 2018, **31**, e3859.

34 H. Mori, S. Jinnai, Y. Hosoda, A. Muraoka, K. Nakayama, A. Saeki and Y. Ie, *Angew. Chem., Int. Ed.*, 2024, **63**, e202409964.

35 Y. He, W. Xu, I. Murtaza, C. Yao, Y. Zhu, A. Li, C. He and H. Meng, *J. Mater. Chem. C*, 2018, **6**, 3683–3689.

36 Y. J. Liu, X. B. Yue, X. H. Wang, Z. Yu, L. W. Lai, G. L. Zhang, A. M. Zhu, Q. G. Zhang and Q. L. Liu, *J. Membr. Sci.*, 2024, **707**, 122998.

37 M. G. Marino, J. P. Melchior, A. Wohlfarth and K. D. Kreuer, *J. Membr. Sci.*, 2014, **464**, 61–71.

38 J. Fan, S. Willdorf-Cohen, E. M. Schibli, Z. Paula, W. Li, T. J. G. Skalski, A. T. Sergeenko, A. Hohenadel, B. J. Frisken, E. Magliocca, W. E. Mustain, C. E. Diesendruck, D. R. Dekel and S. Holdcroft, *Nat. Commun.*, 2019, **10**, 2306.

39 A. Allushi, T. H. Pham, J. S. Olsson and P. Jannasch, *J. Mater. Chem. A*, 2019, **7**, 27164–27174.

40 Y.-J. Shih, Y.-H. Huang and C. P. Huang, *Electrochim. Acta*, 2018, **281**, 410–419.

41 S. Narayanaru, H. Kuroki, T. Tamaki, G. M. Anilkumar and T. Yamaguchi, *RSC Sustain.*, 2025, **3**, 1705–1713.

42 S. Kim, S. H. Yang, S.-H. Shin, H. J. Cho, J. K. Jang, T. H. Kim, S.-G. Oh, T.-H. Kim, H. Han and J. Y. Lee, *Energy Environ. Sci.*, 2024, **17**, 5399–5409.